

Numerical Modeling of Fetch-Limited Waves in the Gulf of Tehuantepec

LEONEL ROMERO AND W. KENDALL MELVILLE

Scripps Institution of Oceanography, University of California, San Diego, La Jolla, California

(Manuscript received 19 August 2008, in final form 22 July 2009)

ABSTRACT

During the Gulf of Tehuantepec Experiment (GOTEX), conducted in February 2004, surface-wave measurements were collected using a scanning lidar [Airborne Topographic Mapper (ATM)] on the National Science Foundation (NSF)/NCAR C-130 aircraft during fetch-limited conditions with winds speeds ranging from 10 to 25 m s⁻¹. The authors present direct comparisons between the observed evolution of the wave field and numerical simulations using a parameterization of the wave energy dissipation. For low and intermediate wavenumbers, the dissipation corresponds to the saturation-based parameterization by Alves and Banner. However, at higher wavenumbers, their formulation cannot maintain saturation of the spectrum. Here, the authors use a dissipation term that forces the spectrum to match the empirical degree of saturation and explicitly balances the wind input and the nonlinear energy fluxes. All model simulations were carried out with “exact” computations of the nonlinear energy transfer because of four-wave resonant interactions and two empirical wind input functions. There is a good agreement for the integral parameters between the observations and the simulations, with root-mean-square (rms) errors between 5% and 12%. The tail of the computed omnidirectional wavenumber spectrum $\phi(k)$ can be approximated by two ranges: an equilibrium range, where $\phi \propto k^{-5/2}$, and a saturation range, where $\phi = \bar{B}k^{-3}$, where \bar{B} is the empirically determined degree of saturation. However, within the equilibrium range, the modeled ϕ overestimates the energy with rms errors between 20% and 50%, and the computed spectra are found to be narrower than the observations by about 10°. Similarly, the modeled bimodal directional distributions, at wavenumbers higher than the spectral peak, exhibit lobe separations and amplitudes that are consistently smaller than the observations. The lobe separation of the bimodal directional distribution for all simulations approximately scales with the square root of the wave age, which is consistent with the observations. The reasons for differences between the measurements and the simulations are discussed.

1. Introduction

Spectral models for deep-water wind waves in the absence of currents are based on the radiative transfer equation,

$$\frac{\partial N(\mathbf{k})}{\partial t} + \mathbf{c}_g \cdot \nabla N(\mathbf{k}) = S_{\text{in}} + S_{\text{nl}} + S_{\text{ds}}, \quad (1)$$

where $N(\mathbf{k})$ is the wave action spectral density, $F(\mathbf{k})/\omega$; $F(\mathbf{k})$ is the directional wavenumber spectrum; ω is the radial frequency; \mathbf{c}_g is the group velocity according to the linear dispersion relationship ($\omega^2 = gk$); g is the gravitational acceleration; S_{in} is the wind input source function; S_{nl} is the nonlinear energy transfer resulting from wave–wave interactions; and S_{ds} corresponds to the

wave action dissipation, primarily resulting from wave breaking. Although our present knowledge of the wind input is far from complete, there are several field and laboratory measurements that give consistent growth rates but with considerable variability. These include the measurements by Snyder et al. (1981), the collation by Plant (1982), and the laboratory and field measurements by Donelan (1987), among others (Badulin et al. 2005). By comparison, the full expression for the nonlinear energy transfer resulting from four-wave resonant interactions has been known for a long time (Hasselmann 1963; Webb 1978; Krasitskii 1994). However, the energy dissipation resulting from wave breaking used in numerical wind-wave models has been formulated based on heuristic physical arguments (Hasselmann 1974), using free parameters, which are tuned numerically by trial and error until the model can reproduce the available observations (Komen et al. 1984; Banner and Young 1994; Alves and Banner 2003, hereafter AB03).

Corresponding author address: Leonel Romero, Scripps Institution of Oceanography, University of California, San Diego, La Jolla, CA 92093-0230.
E-mail: leromero@ucsd.edu

Numerical prediction models that run on a daily basis at global and regional scales, commonly referred to as operational models, are limited to coarse spectral and spatial grids and with parameterizations or approximations of the nonlinear energy fluxes resulting from wave–wave interactions constrained by the computational time available. Thus, present operational wind-wave models can only predict the standard integral parameters, which are the significant wave height and the period and direction of the dominant waves. Because of the large number of operations required, models with good spatial and spectral resolution that use the complete computations of nonlinear energy transfer have been limited to academic investigations (Komen et al. 1984; Banner and Young 1994; AB03; Badulin et al. 2005; Ardhuin et al. 2007). The first study of this kind was by Komen et al. (1984), who focused on the dynamical balance of the spectrum for fully developed seas, using a variant of the dissipation function by Hasselmann (1974). A subsequent study by Banner and Young (1994) showed that the model by Komen et al. (1984) could not reproduce the observations when applied to developing waves under idealized fetch-limited conditions. They concluded that a new dissipation function was needed to improve the model performance. A recent investigation by AB03 proposed a dissipation parameterization that can accommodate several wind input functions with the full computations of S_{nl} . The simulations by AB03 reproduce the integral parameters from field observations over a wide range of fetches, including the asymptotic behavior near full development. However, as shown by Alves et al. (2002), in realistic applications the AB03 dissipation function gave a poor performance when compared to observations, which was mainly attributed to the use of the discrete interaction approximation as a parameterization of the nonlinear energy transfer (Hasselmann and Hasselmann 1985). Moreover, van der Westhuysen et al. (2007) have shown that the AB03 model cannot handle mixed wind-sea and swell conditions. More recently, Ardhuin et al. (2008) have described the problems that arise within the tail of the spectrum when using dissipation models similar to AB03. Recent advances in field measurements of wave-breaking statistics have reported a threshold behavior with respect to the spectral saturation normalized by the directional spreading of the spectrum (Banner et al. 2002), which have been incorporated in a parameterization of spectral dissipation as a modification to the AB03 dissipation function (Banner and Morrison 2006). Because Banner and Morrison (2006) did not provide the necessary information to reproduce their results and it appeared to be a work in progress, their modifications to the AB03 dissipation function (and the wind input) were not considered in this study.

Here, we use an improved dissipation function with two regimes. For low to intermediate wavenumbers, the dissipation parameterization corresponds to the AB03 function. At high wavenumbers, within the saturation range, the dissipation function dynamically forces the spectrum to match the observed degree of saturation and explicitly balances the sum of the wind input and nonlinear transfers. The model was forced with two empirical wind input parameterizations, Snyder et al. (1981) and Yan (1987), and employed the full computations of the nonlinear resonant interactions (Tracy and Resio 1982; van Vledder 2006).

We present a comparison between two-dimensional simulations of spectra and the fetch-limited wind-wave observations collected during the Gulf of Tehuantepec Experiment (GOTEX) in February 2004. The wave observations represent the largest available dataset of wavenumber spectra, with supporting winds and turbulent fluxes, and good directional resolutions over a wide range of fetches, and they are described in detail in Romero and Melville (2010, hereafter RM10). Thus, the GOTEX measurements provide an opportunity to test the AB03 model, with full computations of the nonlinear energy transfer resulting from resonant interactions, under strong wind forcing, beyond comparisons with just the usual integral parameters. All the simulations were carried out using the computational framework of WaveWatch III (WW3), version 2.22 (Tolman 2002).

The structure of the paper is as follows: In section 2, we present an overview of numerical wind-wave models. In section 3, we describe the wind-wave model used for the simulations. In section 4, the two-dimensional simulations over the Gulf of Tehuantepec are compared to the GOTEX observations. The results are summarized and discussed in section 5.

2. Background

State-of-the-art wind-wave models do a very good job of predicting the total energy and peak frequency of the dominant waves under idealized conditions, which include spatially homogeneous and stationary winds blowing over an infinite area or off an infinite straight coastline.

A brief review of the parameterizations used in present wind-wave models is presented here. Hasselmann (1963) derived the first analytical expression of S_{nl} for deep-water waves satisfying the following resonant conditions:

$$\mathbf{k}_1 + \mathbf{k}_2 = \mathbf{k}_3 + \mathbf{k}_4 \quad \text{and}$$

$$\omega_1 + \omega_2 = \omega_3 + \omega_4,$$

where the rate of change of wave action density resulting from all possible four-wave resonant interactions is given by

$$\frac{\partial N_1}{\partial t} = \iiint G(\mathbf{k}_1, \mathbf{k}_2, \mathbf{k}_3, \mathbf{k}_4) \delta(\mathbf{k}_1 + \mathbf{k}_2 - \mathbf{k}_3 - \mathbf{k}_4) \delta(\omega_1 + \omega_2 - \omega_3 - \omega_4) \times [N_1 N_3 (N_4 - N_2) + N_2 N_4 (N_3 - N_1)] d\mathbf{k}_2 d\mathbf{k}_3 d\mathbf{k}_4, \quad (2)$$

where $N_i = N(\mathbf{k}_i)$ is the wave action density at \mathbf{k}_i and G is the interaction coefficient (Hasselmann 1962, 1963; Webb 1978; Krasitskii 1994). It is worth mentioning that nonlinear energy transfer also occurs for nonresonant interactions, but such interactions occur as transients at shorter time scales, which are not important for the slow evolution of the wave field for periods of 10 dominant waves or more (Janssen 2003). The number of calculations required to compute S_{nl} is very large, thus the full solution of S_{nl} has been limited to research applications. Since Hasselmann (1963), there have been many efforts to increase the computational speed of S_{nl} by projecting the six-dimensional integral to three dimensions (Webb 1978). The wave-wave interactions generally transfer energy and momentum from intermediate wavenumbers to both higher and lower wavenumbers (Webb 1978). Most of the transfer is toward lower wavenumbers just before the peak of the spectrum and toward high wavenumbers $\pm 45^\circ$ off the downwind direction. The numerical simulations of Pushkarev et al. (2003) and Banner and Young (1994), using a spectral model that computed S_{nl} exactly, showed that the wavenumber spectrum can develop a bimodal angular distribution at wavenumbers higher than the spectral peak. According to Young and Vledder (1993), four-wave resonant nonlinear interactions are of central importance in the development of the spectrum, smoothing out any perturbation (Resio and Perrie 1991) and controlling the directional spreading.

One of the first effective theories of wind-wave generation was developed by Miles (1957), based on a shear flow instability mechanism through critical-layer interaction of the surface waves and the wave-induced pressure. Following the theoretical framework of Miles, Snyder et al. (1981) examined field measurements of the pressure above the surface waves and reported growth rates much larger than the predictions by the Miles theory. Plant (1982) showed that the available measurements on the wave forcing by wind, from wind-wave tanks and field observations, could be explained with a quadratic dependence on the ratio u_* / c , where u_* is the friction velocity and c is wave speed according to the linear dispersion relation. Yan (1987) proposed a parameterization of the wind input consistent with Snyder et al. (1981) for weakly forced waves, or low values of u_* / c , and approaching the parameterization by Plant (1982), for strongly forced waves. Donelan (1982) showed that the drag coefficient is sea-state dependent. The effects of the

wave-induced stress on the wind input were incorporated in the parameterization by Janssen (1989, 1991) as an extension to the Miles theory. Tolman and Chalikov (1996) introduced a wind input function consistent with Janssen's growth rates but also gave negative input rates for waves traveling faster than the wind or at large angles from the mean wind direction. This parameterization of S_{in} was obtained from numerical simulations of the wave boundary layer over monochromatic waves (Chalikov 1986; Chalikov and Belevich 1993; Burgers and Makin 1993).

The dissipation function S_{ds} is the least understood source function. The first widely used form of S_{ds} was proposed by Hasselmann (1974). It assumes that the loss resulting from wave breaking is linearly related to the spectral density. In contrast, the equilibrium model by Phillips (1985) required a nonlinear form of S_{ds} to balance the other source terms (S_{in} and S_{nl}). The numerical experiments by Komen et al. (1984) showed that a variant of Hasselmann's S_{ds} could balance the source terms for fully developed conditions, producing frequency spectra consistent with the empirical Pierson-Moskowitz spectrum (Pierson and Moskowitz 1964) for fully developed seas. According to Komen et al. (1984), this wind-wave model included a parametric tail, proportional to ω^{-5} at frequencies greater than 2.5 times that at the peak of the spectrum ω_p to give faster computation speeds with no significant effects near the peak of the spectrum. Banner and Young (1994) extended the numerical work of Komen et al. (1984) to test the sensitivity to modifications of the adjustable parameters of S_{ds} and the effect of the prognostic tail on the energy-containing region of the spectrum. They performed fetch-limited numerical experiments using as diagnostics the Joint North Sea Wave Project (JONSWAP) fetch relations (Hasselmann et al. 1973), the high-frequency spectral slope and energy level of Banner (1990), and the directional spreading of Donelan et al. (1985). Their results showed that the evolution of the spectrum was sensitive to the prognostic tail and that the model was not able to reproduce the JONSWAP observations regardless of the modifications made to the free parameters of S_{ds} . The conclusion was that an alternate form of S_{ds} is required to reproduce the observations. A recent study by AB03 proposed a saturation-based nonlinear form of S_{ds} . Their numerical experiments showed an improvement, reproducing the integral parameters and the high-wavenumber spectral shape and energy density of the spectrum. However, they

could not accurately reproduce the empirical bimodal distribution for fully developed seas reported by Hwang et al. (2000).

3. Wind-wave model

In this study, WW3, version 2.22, is used as the numerical framework to carry out the numerical wind-wave simulations. WW3 was developed at the National Centers for Environmental Prediction (NCEP; Tolman 2002) and is used operationally to produce global and regional forecasts on a daily basis at NCEP and at the Fleet Numerical Meteorology and Oceanography Center (FNMOC). The source code is written in Fortran 90, and is fully parallelized to work across multiple processors with the Message Passing Interface (MPI).

The model has several explicit propagation schemes available. Following AB03, we used the first-order upwind scheme with fine spatial, temporal, and spectral resolutions. For the time step integration, the default semi-implicit scheme without limiters was used for all the simulations presented here. Integration limiters are commonly used in wind-wave model simulations to ensure numerical stability by limiting the maximum change in energy or action density at each spectral component. To avoid any artificial effects on the shape of the spectrum, the integration limiters were turned off, but the solutions were free of integration instabilities at all times.

The model grid is in the frequency domain, in polar coordinates (ω, θ) , with a constant bandwidth $(d\omega/\omega = \text{constant})$. In this study, the model spectra produced from the simulations were converted to the wavenumber domain (k, θ) using the linear dispersion relationship for deep-water waves,

$$F(k, \theta) = \frac{1}{k} \frac{\partial \omega}{\partial k} \varphi(\omega, \theta), \quad (3)$$

$$= \frac{g^{1/2}}{2k^{3/2}} \varphi(\omega, \theta), \quad (4)$$

where φ is the directional frequency spectrum.

a. Source functions

All simulations were carried out with exact computations of the nonlinear energy transfer resulting from four-wave resonant interactions using the Webb–Resio–Tracy algorithm (Webb 1978; Tracy and Resio 1982) adapted by van Vledder (2006; version 5). The computations of S_{nl} use a parametric tail of the form $\varphi(\omega, \theta) \sim \omega^{-5}$, or $F(k, \theta) \sim k^{-4}$, for frequencies larger than 0.75 times the maximum resolved frequency.

The wind input parameterizations used are Snyder et al. (1981) and Yan (1987)—referred to as S_{in}^S and S_{in}^Y , respectively—which are given by

$$S_{\text{in}}^S = 0.25 \frac{\rho_a}{\rho_w} \left(\frac{28u_*}{c} \cos\theta - 1 \right) N(k, \theta)w \quad \text{and} \quad (5)$$

$$S_{\text{in}}^Y = \left[0.04 \left(\frac{u_*}{c} \right)^2 + 0.00544 \frac{u_*}{c} + 0.000055 \right] \cos\theta - 0.00031 \Big] N(k, \theta)w, \quad (6)$$

where $\rho_a = 1 \text{ kg m}^{-3}$ and $\rho_w = 1.25 \times 10^3 \text{ kg m}^{-3}$ are the air and water densities, respectively; u_* is the friction velocity of the air; and c is the wave phase speed according to the linear dispersion relationship. Both functions of S_{in} give comparable growth rates for long, weakly forced waves, but S_{in}^Y is larger than S_{in}^S for short, strongly forced waves, giving growth rates comparable to Plant (1982).

In this study, the dissipation function S_{ds} is parameterized with a two-phase behavior and is defined as

$$S_{\text{ds}}(k, \theta) = Y_l(k)S_{\text{ds}}^l(k, \theta) + Y_h(k)S_{\text{ds}}^h(k, \theta), \quad (7)$$

where S_{ds}^l and S_{ds}^h correspond to the dissipation at low and high wavenumbers, respectively. The functions Y_l and Y_h act as a switch enabling the dissipation in different the parts of the spectrum (for details on the implementation, see appendix A).

Following AB03, the dissipation function for low and intermediate wavenumbers is defined as

$$S_{\text{ds}}^l(k, \theta) = -C_{\text{ds}} \left[\frac{B(k)}{B_r} \right]^{p/2} (E_{\text{tot}} k_p^2)^m \left(\frac{k}{\bar{k}} \right)^n N(k, \theta)\omega, \quad (8)$$

where $B(k) = \phi(k)k^3$ is the azimuth-integrated saturation. With

$$\phi(k) = \int_{-\pi}^{\pi} F(k, \theta)k d\theta, \quad (9)$$

the total energy density or variance is given by

$$E_{\text{tot}} = \langle \eta^2 \rangle = \int_{k_o}^{k_f} \phi(k) dk, \quad (10)$$

where E_{tot} is the energy density or sea surface mean square elevation $\langle \eta^2 \rangle$; with the brackets representing a spatial or temporal average. The lower and upper limits of the spectral grid are k_o and k_f , respectively. The wavenumber component at the spectral peak is k_p ; the mean wavenumber component

TABLE 1. One-way nested grid configuration for one-dimensional simulations, where X_o corresponds to the initial location of each grid; Δx is the spatial resolution; Δt_p and Δt_s are time step increments for the spatial propagation and source term integration, respectively; N_x is the number of spatial grid points; and CFL is the Courant–Friedrichs–Levy number. The spectral grid had a directional resolution of 4.5° between 0° and 360° and a constant bandwidth $d\omega/\omega = 0.078$, or $dk/k = 0.156$ according to the linear dispersion relationship, with a range of resolved frequencies between 0.443 and $12.064 \text{ rad s}^{-1}$ (or between 0.02 and 14.85 rad m^{-1}) having a total of 45 components in ω and 80 in direction.

Grid No.	X_o (km)	Δx (km)	Δt_p (s)	Δt_s (s)	N_x	CFL
1	1.0	0.1	3	300	64	0.33
2	7.3	0.5	19	300	64	0.42
3	38.8	1.0	39	450	64	0.43
4	101.8	2.0	79	500	64	0.44
5	227.8	3.0	110	600	64	0.41
6	416.8	4.0	110	900	64	0.30
7	668.8	5.0	110	900	64	0.24

$$\bar{k} = \frac{\int_{k_o}^{k_f} \phi(k) k dk}{E_{\text{tot}}}; \quad \text{and} \quad (11)$$

$$p = \frac{p_o}{2} \left\langle 1 + \tanh \left\{ 10 \left[\frac{B(k)}{B_r} \right]^{1/2} - 1 \right\} \right\rangle, \quad (12)$$

which is a function between 0 and 1 that enables the saturation dependence of S_{ds} for $B(k) > B_r$.

The AB03 dissipation function can give a good development of the integral parameters for fetch-limited waves, but it produces an imbalance in the high-wavenumber part of the spectrum (Ardhuin et al. 2008), giving rise to

a sudden roll-off in the tail of the spectrum (see, e.g., Romero 2008; Babanin and van der Westhuysen 2008). To improve the behavior on the tail of the spectrum, we consider the work by Phillips (1985), who derived an expression for the rate of energy dissipation within the equilibrium range, where $\phi \propto k^{-5/2}$, by balancing source terms such that

$$|S_{\text{in}}| \propto |S_{\text{ds}}| \propto |S_{\text{nl}}| \quad \text{and} \quad (13)$$

$$S_{\text{in}} + S_{\text{ds}} + S_{\text{nl}} = 0. \quad (14)$$

However, the GOTEX data suggest that the omnidirectional wavenumber spectra can be approximated by two power laws: a spectral slope of $k^{-5/2}$ followed by a slope of k^{-3} . Thus, the equilibrium range model by Phillips (1985) would only apply to intermediate scales where $\phi \propto k^{-5/2}$. Moreover, it has been shown in several numerical investigations (van Vledder 2006; Lavrenov 2001; Resio and Perrie 1991) that the computations of S_{nl} for a realistic wave spectrum, such as the JONSWAP spectrum, can be approximated by a three-lobe structure with alternating signs: a positive lobe at wavenumbers lower than the spectral peak, a negative lobe at intermediate scales, and another positive lobe at high wavenumbers. By definition, the equilibrium range model by Phillips (1985) cannot apply across zero crossings of S_{nl} nor in the limit as $S_{\text{nl}} \rightarrow 0$. Thus, the zero-up crossing k_{zu} of the azimuth-integrated nonlinear energy fluxes is used as the reference scale to separate the two dissipation regimes (see details in appendix A).

The high-wavenumber dissipation is defined as

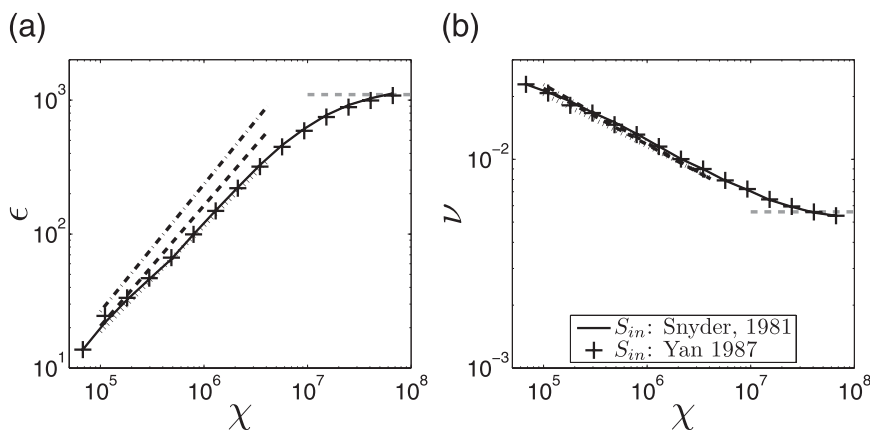


FIG. 1. (a) Nondimensional energy ϵ and (b) peak frequency ν vs nondimensional fetch χ . The solid black lines and crosses correspond to one-dimensional simulations using the wind input functions by Snyder et al. (1981) and Yan (1987), respectively. The dotted, dashed, and dashed-dotted lines correspond to the reanalysis by Kahma and Calkoen (1992) for stable, neutral, and unstable conditions, respectively. The gray lines correspond to the Pierson–Moskowitz limits of the spectrum (Komen et al. 1984).

TABLE 2. Spectral dissipation parameters used for the numerical simulations. (Parameters are dimensionless.)

S_{in}	C_{ds}	B_r	p_o	m	n	Comments
Snyder et al. (1981)	9.0×10^{-4}	2.0×10^{-3}	3.0	0.50	0.50	Stable atmospheric stratification
Yan (1987)	9.36×10^{-4}	2.25×10^{-3}	4.0	0.50	0.75	Stable atmospheric stratification

$$S_{ds}^h(k, \theta) = -H(B)[S_{in}^h(k, \theta) + S_{nl}(k, \theta)], \quad (15)$$

where H is a function that enhances or reduces the dissipation as the omnidirectional saturation $B(k) = \phi(k)k^3$ deviates from the empirical value \bar{B} (RM10). As $B \rightarrow \bar{B}$, $H \rightarrow 1$ and $S_{ds}^h \rightarrow -(S_{in} + S_{nl})$, explicitly enforcing the source term balance. The details on the implementation and stability of the saturation balance are described in appendix A.

b. One-dimensional implementation

The main goal of this study is to compare the fetch-limited wind-wave observations against two-dimensional numerical simulations with good spectral resolution. For fetch-limited simulations, the limitation imposed by the computations of S_{nl} requires the use of nested grids. The dissipation model was tuned in a one-way nested configuration of one-dimensional fetch-limited runs (see grid details in Table 1), with a spatial resolution that gradually decreased with increasing fetch. The total energy and dominant frequency were adjusted against the fetch relationships by Kahma and Calkoen (1992) for a stably stratified atmospheric boundary layer. This is justified, because the stability of the boundary layer during GOTEX was typically stable at short to intermediate fetches and unstable at long fetches. For more details on the nesting procedure, see Romero (2008). The simulations were initialized with a JONSWAP spectrum

TABLE 3. One-way nested grid configuration for two-dimensional simulations over the Gulf of Tehuantepec. The terms Lat_o and Lon_o correspond to the initial location of each grid; Δx and Δy correspond to the spatial resolution; Δt_p and Δt_s are time step increments for the spatial propagation and source term integration, respectively; N_x and N_y are the number of spatial grid points in each direction; and CFL is the Courant–Friedrichs–Levy number. The spectral grid had a directional resolution of 4.5° between 0° and 360° and a constant bandwidth $d\omega/\omega = 0.078$, or $dk/k = 0.156$ according to the linear dispersion relationship, with a range of resolved frequencies between 0.263 and 14.066 rad s^{-1} (or between 0.007 and 20.188 rad m^{-1}) having a total of 54 components in ω and 80 in direction.

Grid No.	Lat_o ($^\circ$)	Lon_o ($^\circ$)	$\Delta x, \Delta y$ (km)	Δt_p (s)	Δt_s (s)	N_x	N_y	CFL
1	16°07'07"	−95°22'64"	0.5	19	285	22	290	0.71
2	16°02'00"	−95°46'30"	1.4	55	285	18	162	0.73
3	15°50'40"	−96°32'09"	3.0	119	285	22	130	0.74
4	15°19'55"	−97°48'00"	4.5	140	285	18	82	0.68
5	15°11'07"	−98°30'00"	5.5	150	285	34	82	0.51

with the bimodal directional distribution by Ewans (1998). Following Lewis and Allos (1990), the nondimensional energy and peak frequency were adjusted to match the composite growth curves by Kahma and Calkoen (1992) for a stable atmospheric stratification, at short to intermediate fetches, and the Pierson–Moskowitz limits (Komen et al. 1984), at long fetches.

Figure 1 shows the nondimensional energy and peak frequency versus the nondimensional fetch from one-dimensional simulations carried out with S_{in}^S (solid black line) and S_{in}^Y (crosses). Both models approximately agree with the Kahma and Calkoen (1992) fetch relationships for stable conditions and approaching the Pierson–Moskowitz limits at long fetches. The nondimensional frequency in both models overshoots the Pierson–Moskowitz limit within a small error. Additional experiments showed that a better adjustment of the modeled peak frequency against the empirical data would result in larger errors for the total energy near full development. The adjusted dissipation parameters are shown in Table 2.

4. Two-dimensional simulations

In this section, we present a direct comparison between the Airborne Topographic Mapper (ATM) wind-wave observations of fetch-limited wavenumber spectra,

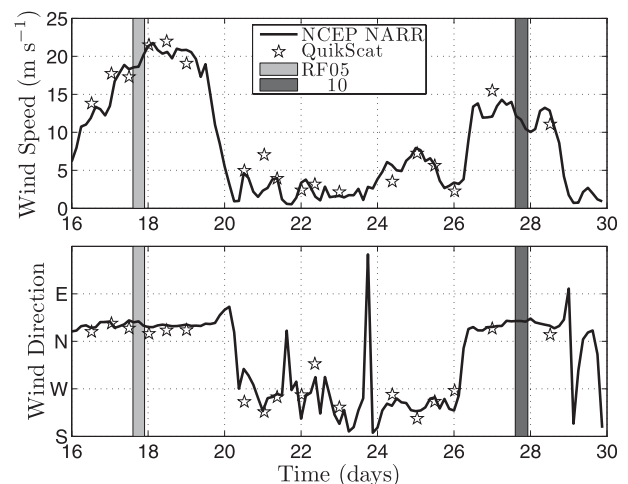


FIG. 2. Time history of wind speed and direction at 15°N , 95°W in the Gulf of Tehuantepec. The solid black line corresponds to NCEP/NARR model wind data, and the stars are the scatterometer winds. The duration of RFs 05 and 10 are shown with solid gray bars.

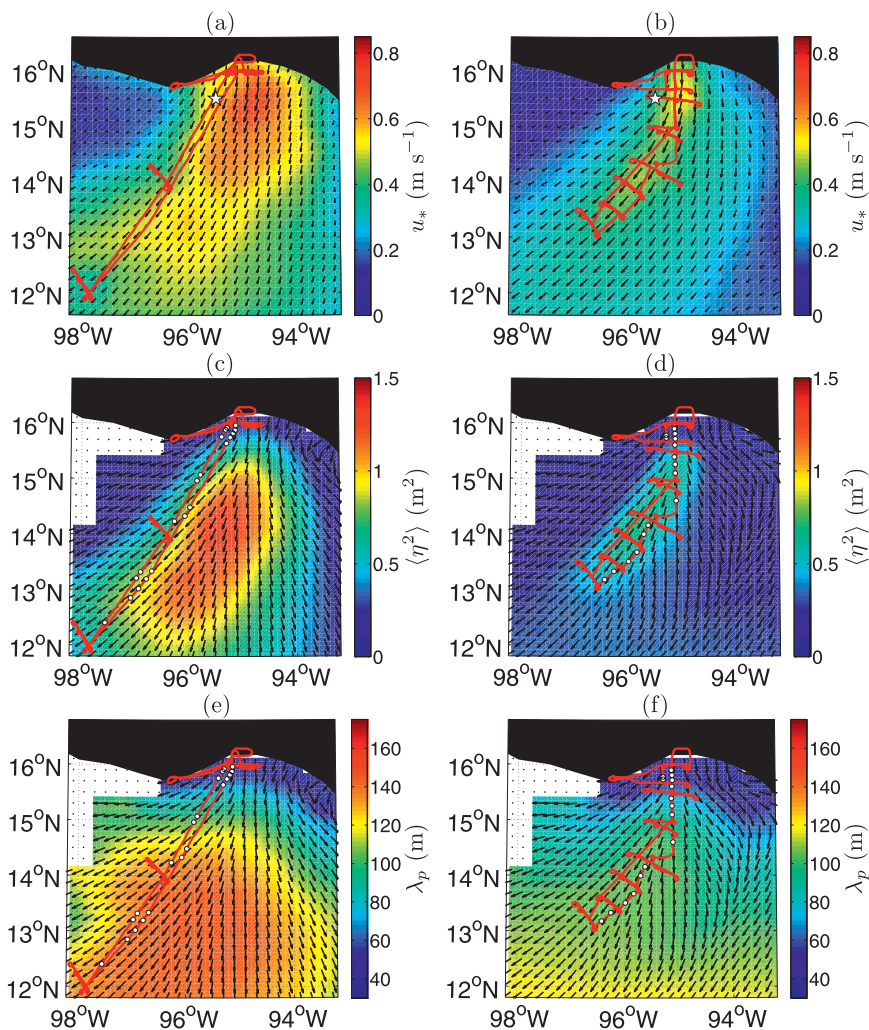


FIG. 3. RFs (left) 05 and (right) 10. (a),(b) Objective maps of friction velocity (u_*) used to drive the two-dimensional simulations, with the solid lines showing the wind direction. The white stars correspond to the location of the time series shown in Fig. 2. (c),(d) The energy densities and (e),(f) the wavelengths of the dominant waves from two-dimensional simulations forced with S_m^0 . The black arrows indicate the dominant wave direction. The wave energy and wavelength were bin averaged over a regular grid for visual clarity. The solid red lines indicate the flight tracks. The white circles indicate the location of the ATM observations.

collected by RM10 during GOTEX, and two-dimensional simulations with good spectral resolution (for details, see Table 3). The two research flights (RFs) considered for this comparison are RF 05 and 10, when the environmental conditions were closest to idealized fetch-limited seas.

The two-dimensional simulations were carried out with a procedure similar to the one used for the one-dimensional simulations, in section 3, using a one-way nested configuration with high spatial resolution near shore, gradually decreasing with increasing fetch (see also Table 3). All model runs were initialized with a JONSWAP spectrum and Ewans (1998) bimodal directional distribution. The simulation for RF 05 forced

with the wind input by Snyder et al. (1981) was initialized with energy densities and peak frequencies of the simulation for RF 05 with wind input by Snyder et al. (1981) set longitudinally homogenous, varying only with latitude approximately matching the ATM observations along the flight path. All other simulations were initialized with the fetch relations from RM10, using the local winds and the fetch estimated as the latitudinal distance between a given point and the shoreline at (16°11'7"N). The latter initialization resulted in a faster convergence toward a steady solution. Additional experiments demonstrated that the different initial conditions give negligible differences on the results.

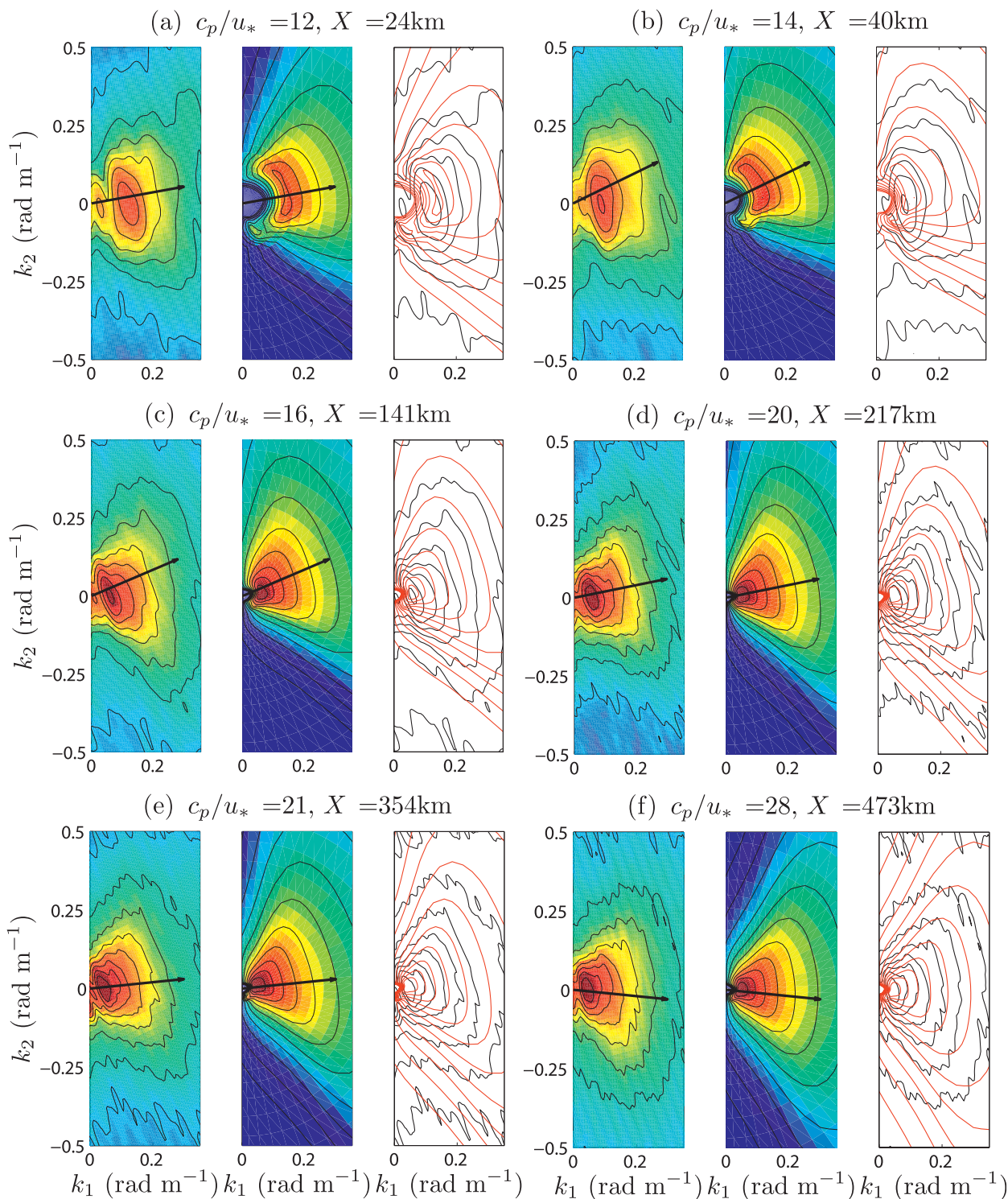


FIG. 4. Comparison of measured and simulated directional wavenumber spectra in logarithmic scales for RF 05. The corresponding effective fetches X are (a) 24, (b) 40, (c) 141, (d) 217, (e) 354, and (f) 473 km. The black arrows indicate the local wind direction. The numerical simulations correspond to runs for stable atmospheric stratification using the wind input by Snyder et al. (1981).

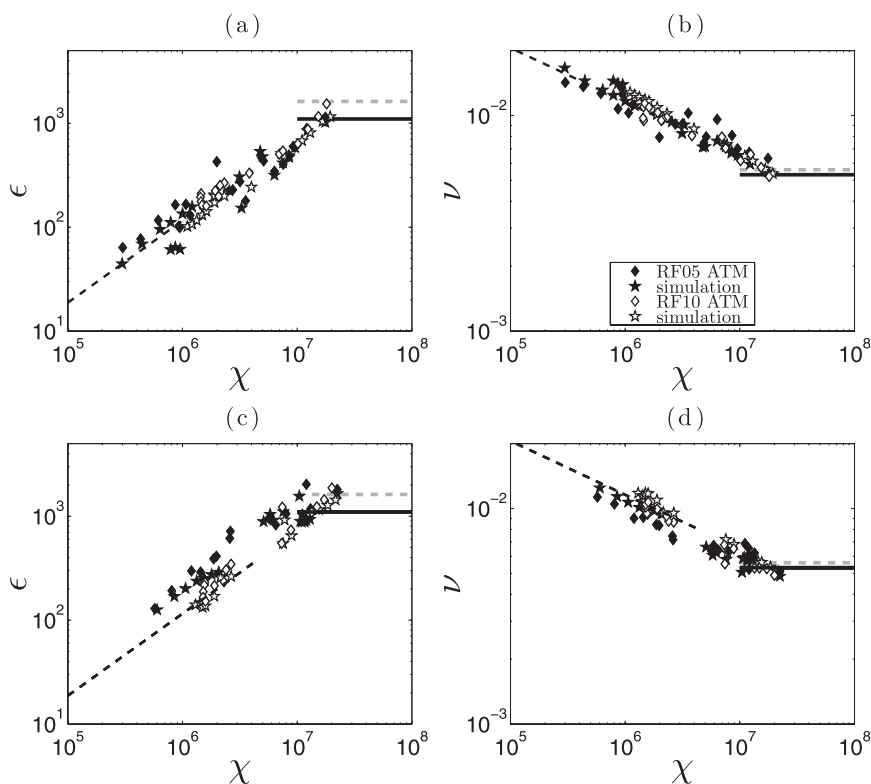


FIG. 5. (left) Nondimensional energy ϵ and (right) spectral peak frequency ν vs nondimensional effective fetch χ . The data scaled with the (a),(b) measured and (c),(d) mapped velocities. The diamonds correspond to the ATM measurements. The stars correspond to the two-dimensional simulations forced with S_m^s . The dashed black lines correspond to the reanalysis by Kahma and Calkoen (1992) for stable atmospheric stratification. The solid black and dashed gray lines correspond to the limits for a Pierson-Moskowitz spectrum (Komen et al. 1984) and by Alves et al. (2003), respectively.

a. Winds

The two-dimensional simulations for RFs 05 and 10 were forced with friction velocity fields calculated from an objective analysis (Bretherton et al. 1976) that combines the low-level measurements, collected onboard the National Science Foundation/National Center for Atmospheric Research (NSF/NCAR) C-130 aircraft, and the available Quick Scatterometer (QuikSCAT) winds or model winds from the NCEP North American Regional Reanalysis (NARR). The QuikSCAT data are available from the National Aeronautics and Space Administration (NASA) Jet Propulsion Laboratory (available online at <http://poet.jpl.nasa.gov/>). The measured friction velocities from low-level flights (30–50-m altitude) were assumed to be in a constant momentum flux layer. As discussed by RM10, the analysis of the GOTEX measurements reported by Friehe et al. (2006) showed stress divergence near the shore, which was in balance with the pressure gradient; however, the scatter of the stress profiles was greater than the expected change resulting

from extrapolation of the stress to the surface. NCEP/NARR winds have a relatively coarse resolution in space and time of 32 km and 3 h, respectively. The QuikSCAT product used has a spatial resolution of 25 km, and over the Gulf of Tehuantepec the satellite can have from zero to two passes per day. Following Perlín et al. (2004), the scatterometer neutral 10-m wind velocities were inverted back to friction velocities using the drag coefficient given by Large and Pond (1982), as were the NCEP/NARR 10-m winds. The objective maps were calculated assuming an isotropic decorrelation length of 50 km, which is comparable to the downwind spatial resolution of the measured wind stress and is also reasonable given the coarseness of the scatterometer and model winds as well as the fact that the mountain gap, at the Tehuantepec isthmus, is only 30 km wide. Each simulation was forced with the mapped friction velocity assuming steady wind conditions. Figure 2 shows the time history of the wind at (15°N, 95°W). For geographical reference, see Fig. 3.

For the calculations of the objective map of friction velocities for RF 05, there are two QuikSCAT passes

TABLE 4. The rms errors of simulated spectra against the ATM observations for the significant wave height ($H_s = 4\sqrt{E_{tot}}$), dominant wave period T_p , dominant wave direction θ_p , and mean compensated spectra $\langle \phi k^{5/2} \rangle$ and $\langle \phi_1 k_1^3 \rangle$, where the brackets represent a spectral average for $2.25k_p < k < 0.35 \text{ rad m}^{-1}$ according to Eqs. (A1) and (34) in RM10.

RF	S_{in}	H_s (%)	T_p (%)	θ_p (%)	$\langle \phi k^{5/2} \rangle$	$\langle \phi_1 k_1^3 \rangle$
5	Snyder et al. (1981)	5	10	8	26	52
10	Snyder et al. (1981)	12	8	10	54	101
5	Yan (1987)	7	12	6	20	37
10	Yan (1987)	12	7	10	32	63

over the Gulf of Tehuantepec, one at 0600 LT and the other at 1800 LT, corresponding to 1 h prior to and 4 h after the ATM data acquisition period. Both scatterometer passes were averaged together, weighted toward 0900 LT, corresponding to the average time of the ATM data acquisition. The scatterometer data and the measured friction velocities from low-altitude flights (at about 50 m above mean sea level) were used to produce an objective map (see Fig. 3a), which was used as input for the two-dimensional simulations.

For RF 10, the QuikSCAT data available are limited to a single pass and miss most of the area of interest. However, the friction velocity measurements collected on board the NSF/NCAR C-130 aircraft had a good spatial coverage of the wind jet. For the objective analysis, the measured friction velocity was combined with NCEP/NARR model data to produce an average wind map for

the simulations. The NCEP/NARR model data were averaged between 0400 and 1600 LT, then converted to friction velocities using the Large and Pond (1982) drag coefficient, and combined with the friction velocity measurements to estimate an objective map. During the mapping procedure, the friction velocity measurements were weighted more heavily, by a factor of 4, than the model winds. Figures 3a,b show the friction velocity maps used for the two-dimensional simulations of RFs 05 and 10.

b. Directional spectra

Figure 4 shows a sample comparison between various measured and simulated two-dimensional wavenumber spectra for RF 05 using S_{in}^S , from short (24 km) to very long fetches (473 km). The simulated spectra are always narrower than the observations, particularly near the spectral peak. However, the overall development of the computed spectrum with increasing fetch is similar to that from the observations.

c. Integral parameters

In this section we present a direct comparison of the standard integral parameters, the energy density and wavenumber at the spectral peak, between the measurements and the simulations. The spatial distributions of the integral parameters for RFs 05 and 10 from the simulations forced with S_{in}^S are shown in Figs. 3c-f. Figure 5 compares the measured and computed non-dimensional energy density,

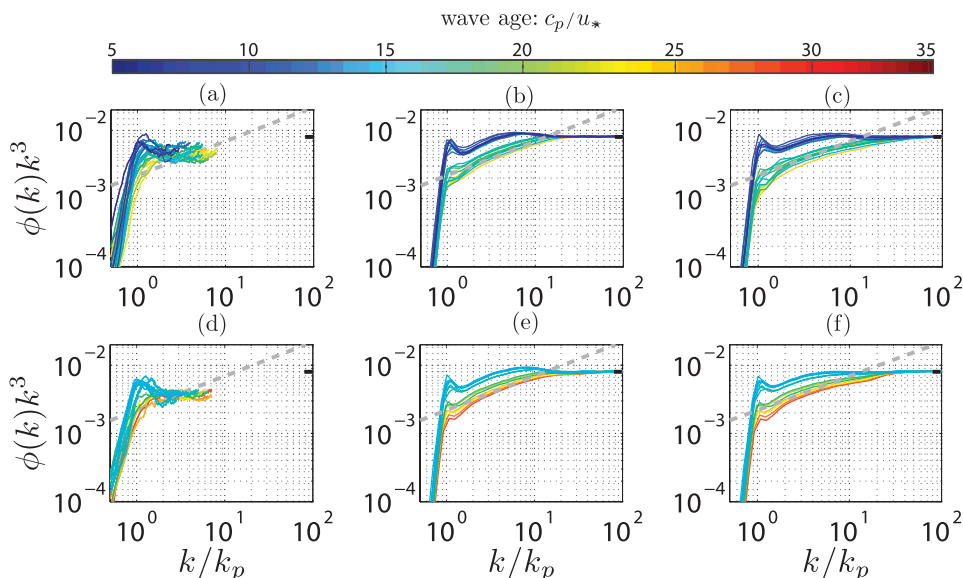


FIG. 6. Compensated omnidirectional spectra for RFs (top) 05 and (bottom) 10: (a),(d) the ATM observations and the two-dimensional simulations using (b),(e) S_{in}^S and (c),(f) S_{in}^V as wind input. The dashed gray line is a reference spectral slope proportional to $k^{1/2}$, and the horizontal black tick mark shows the degree of saturation reported by RM10.

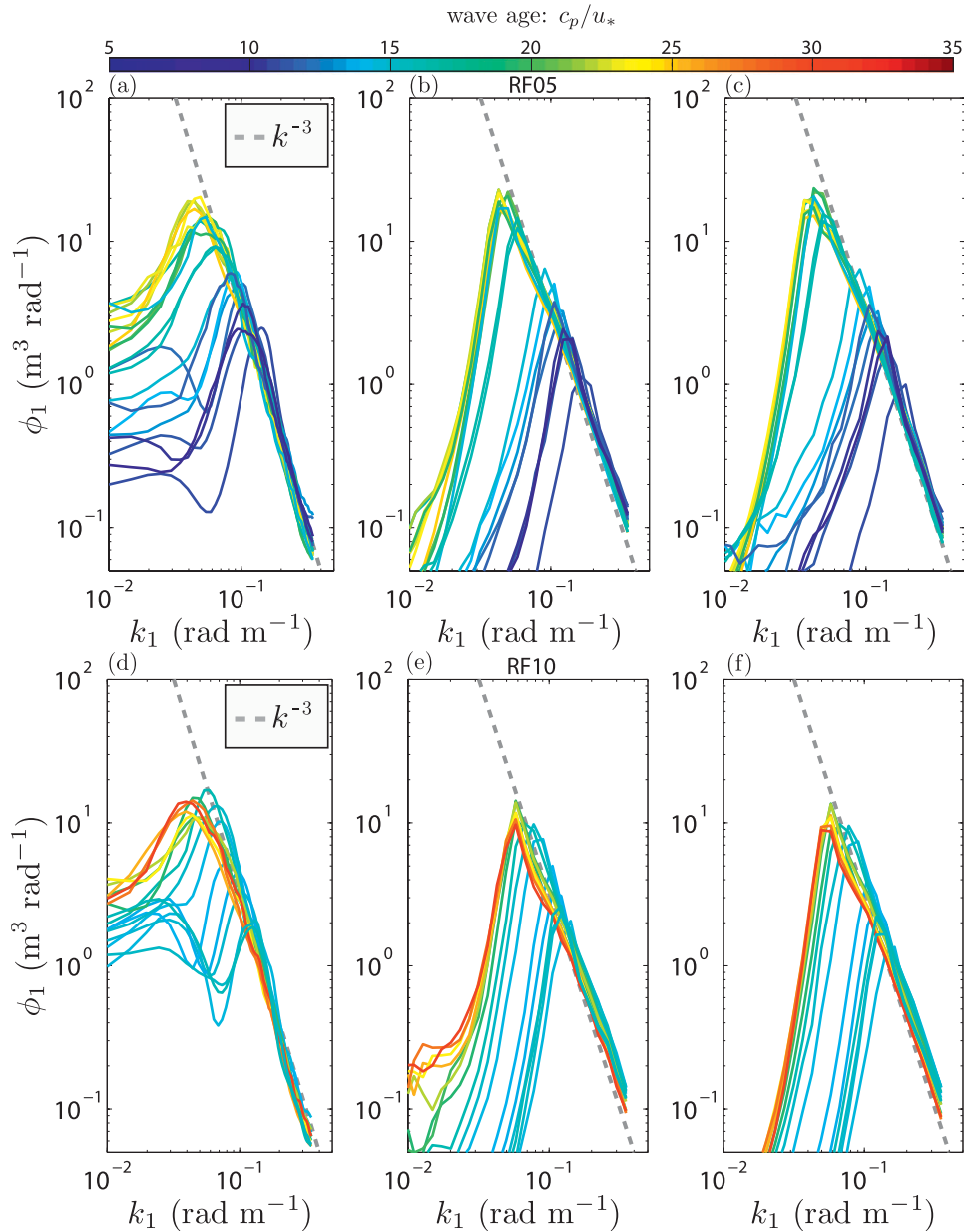


FIG. 7. One-dimensional k_1 spectra for RFs (top) 05 and (bottom) 10 for (left) the ATM observations and the computed spectra from two-dimensional simulations forced with (middle) S_m^S and (right) S_m^Y .

$$\epsilon = \frac{\langle \eta^2 \rangle g^2}{u_{*e}^4}, \quad (16)$$

$$\chi = \frac{X_e g}{u_{*e}^2}, \quad (18)$$

and peak frequency,

$$\nu = \frac{f_p u_{*e}}{g}, \quad (17)$$

plotted versus the nondimensional effective fetch,

where u_{*e} and X_e are the effective friction velocity and fetch, respectively (see RM10). The nondimensional parameters in Fig. 5 are scaled with the friction velocity from both the measurements (top panel) and the objective maps (bottom panel). The friction velocities from the objective maps are more comprehensive and on average smaller in magnitude than the instantaneous

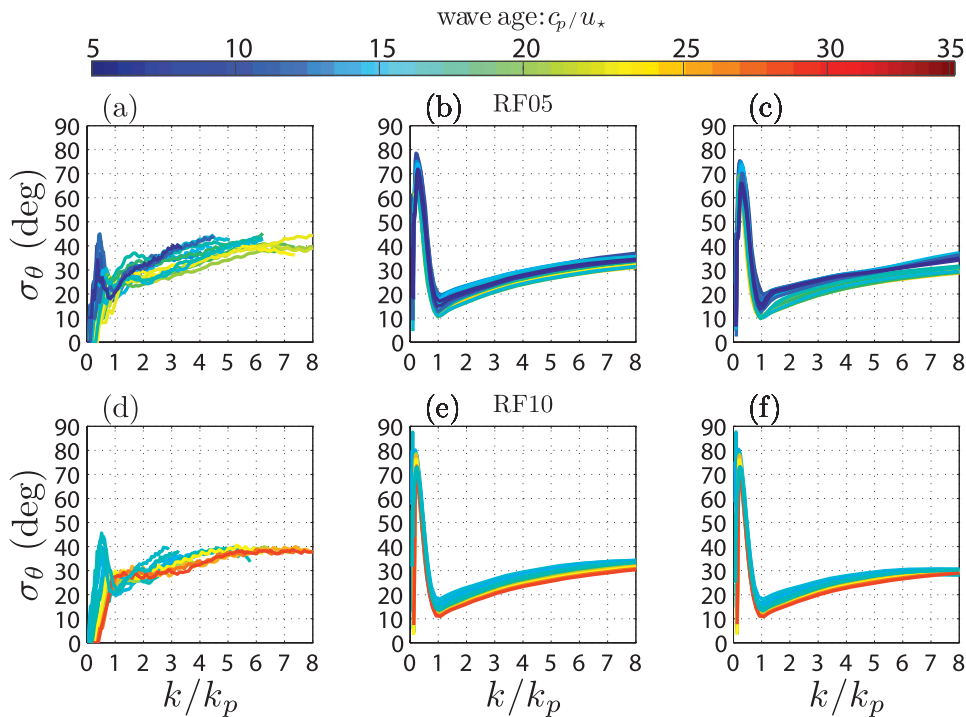


FIG. 8. Directional spreading σ_θ for RFs (top) 05 and (bottom) 10 for (left) the ATM observations and the computed directional spreading from two-dimensional simulations forced with (middle) S_{in}^S and (right) S_{in}^Y .

measurements. The computations in Fig. 5 correspond to simulations forced with S_{in}^S . The results of the simulations using S_{in}^Y gave nearly identical results and are omitted for clarity. Regardless of the scaling velocity used to nondimensionalize the data, the model and measurements are in good agreement. At long fetches, the model nondimensional energy, scaled with the mapped friction velocity, exceeds the expected limiting value at full development, suggesting that at such fetches the spectrum is locally overdeveloped because of the decreasing winds with increasing fetch effectively becoming a young swell leaving the generation site. In general, the simulated significant wave height, dominant wave period, and dominant wave direction are in good agreement with the observations, with root-mean-square errors between 5% and 12%, as shown in Table 4.

d. One-dimensional spectra

Figure 6 shows the development of the compensated azimuth-integrated spectra $\phi(k)k^3 = \int_{-\pi}^{\pi} F(k, \theta)k^4 d\theta$ from the ATM observations (Figs. 6a,d) and the two-dimensional simulations (Figs. 6b,c,e,f). In general, both the measured and simulated spectra show that at intermediate wavenumbers ϕ is approximately proportional to $k^{-5/2}$, but the energy density from the simulations is on average larger than the observations, with root-mean-square (rms) errors between 20% and 50%, as

shown in Table 4. At higher wavenumbers, the computed spectra show a power-law transition to $\phi \propto k^{-3}$, matching the observed degree of saturation by RM10.

In Cartesian coordinates, the one-dimensional k_1 spectra shown in Fig. 7 are defined as

$$\phi_1(k_1) = \int_{-0.5}^{0.5} F(k_1, k_2) dk_2, \quad (19)$$

where $\mathbf{k} = (k_1, k_2) = (k, \theta)$ is the two-dimensional wavenumber in Cartesian and polar coordinates, and the unit vector \hat{k}_1 and $\theta = 0^\circ$ correspond to the dominant wave direction. At wavenumbers sufficiently greater than the spectral peak, for both the data and the simulations, ϕ_1 is approximately proportional to k_1^{-3} . However, the relative difference between the computations and the observations is significant, giving rms errors for the mean compensated spectrum within 40%–100% (see Table 4).

e. Other moments of the spectrum

Banner and Young (1994) define the directional spreading using the first spectral moment over half of the direction spectrum. This can be generalized as

$$\sigma_\theta(k) = \frac{\int_{-\pi/2}^{\pi/2} F(k, \theta)|\theta| d\theta}{\int_{-\pi/2}^{\pi/2} F(k, \theta) d\theta}, \quad (20)$$

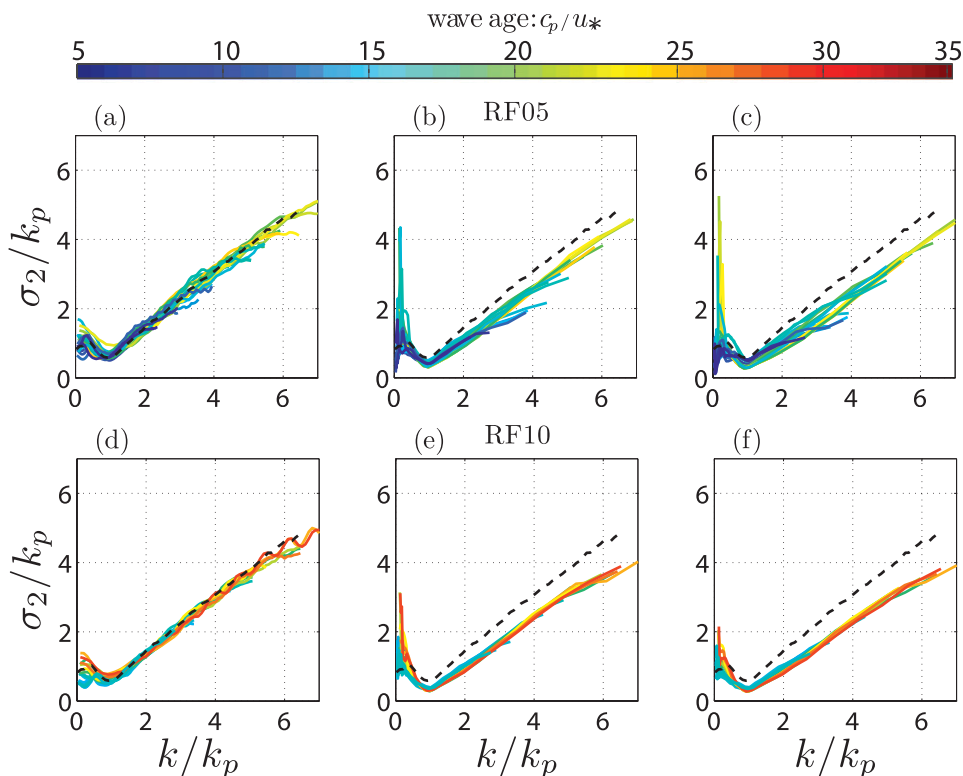


FIG. 9. Normalized spectral width in the direction orthogonal to the dominant waves (σ_2/k_p) vs k/k_p for RFs (top) 05 and (bottom) 10 for (left) the ATM observations and the simulated spectral width from two-dimensional simulations forced with (middle) S_{in}^S and (right) S_{in}^Y .

where $\theta = 0^\circ$ corresponds to the dominant wave direction, providing a measure of the average half-width of the spectrum. Figure 8 shows the directional spreading for RFs 05 and 10. Figures 8a,d correspond to the observations, and Figs. 8b,e and 8c,f show the spreading from the computed spectra using S_{in}^S and S_{in}^Y , respectively. Both the measured and computed spectra are narrowest near the spectral peak, broadening toward both lower and higher wavenumbers. As expected from the comparisons of directional spectra shown in Fig. 4, the simulations are consistently narrower than the observations by about 10° – 15° .

RM10 proposed another metric to characterize the lateral spreading of the spectrum: the width of the spectrum in the direction orthogonal to the dominant wave direction as given by

$$\sigma_2(k_1) = \left[\frac{\int_{-0.5}^{0.5} F(k_1, k_2) k_2^2 dk_2}{\int_{-0.5}^{0.5} F(k_1, k_2) dk_2} \right]^{1/2}, \quad (21)$$

where the limits of integration are in radians per meter and were set according to the resolution of the observations as discussed in RM10. Figure 9 shows σ_2/k_p

versus k_1/k_p for the observations (Figs. 9a,d) and the simulations using S_{in}^S (Figs. 9b,e) and S_{in}^Y (Figs. 9c,f). According to this metric (σ_2), both the models and the observations show a self-similar behavior, but the model spectra are consistently narrower than the observations.

f. The bimodal distribution

Direct comparisons between the measured and modeled directional distributions are shown in Fig. 10. The directional wind-wave spectra at wavenumbers higher than the spectral peak, for both model and measured spectra, exhibit bimodal distributions, with maxima around 30° – 40° from the dominant wave direction. The lobe separation and amplitude are on average larger for the younger waves (Fig. 10), for both simulated and measured spectra. Following Hwang et al. (2000), the bimodal distribution can be characterized through the azimuthal lobe separation and relative amplitude given by

$$\theta_{\text{lobe}}(k) = \frac{|\theta_1(k)| + |\theta_2(k)|}{2} \quad \text{and} \quad (22)$$

$$r_{\text{lobe}}(k) = \frac{1}{2} \frac{F(k, \theta_1) + F(k, \theta_2)}{F(k, 0)}, \quad (23)$$

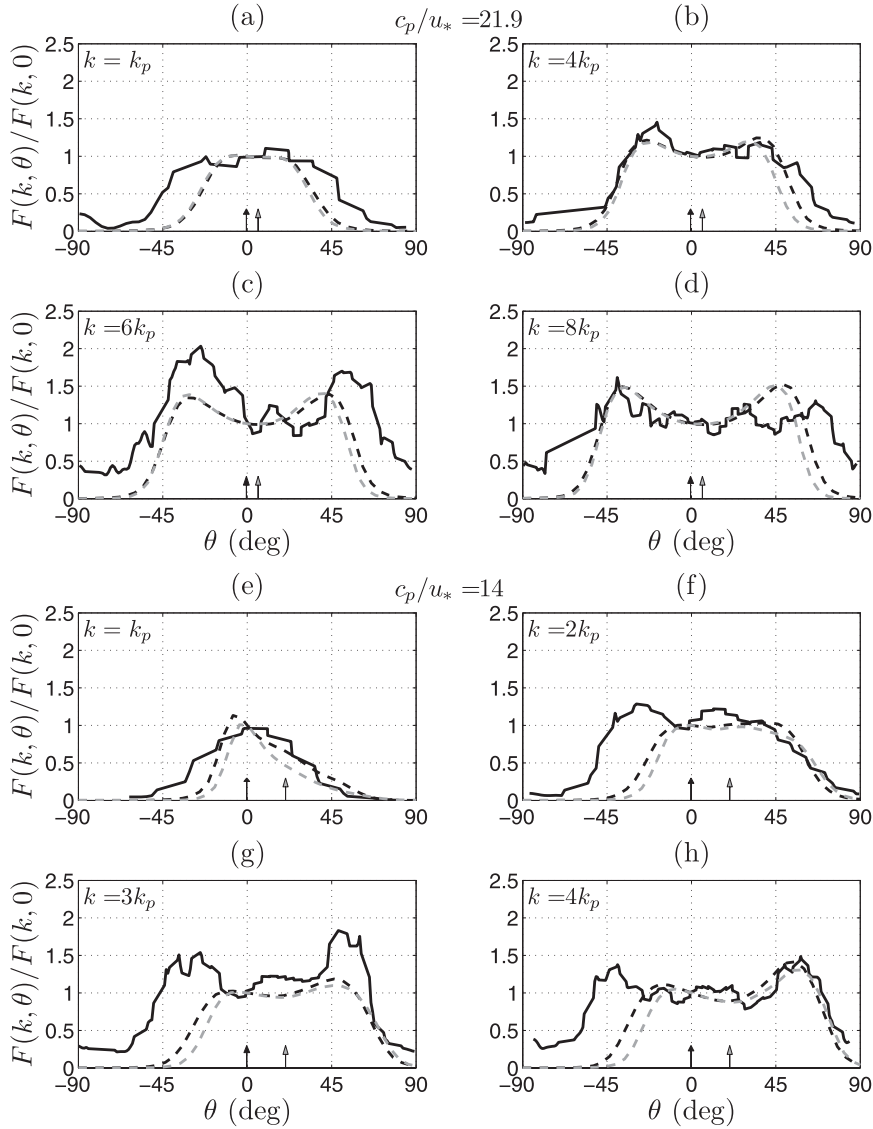


FIG. 10. Sample comparisons between observed (solid black line) and simulated (dashed lines) normalized directional distribution of the spectrum, $F(k, \theta)/F(k, 0)$, where $\theta = 0^\circ$ corresponds to the dominant wave direction. The local wave ages (c_p/u_*) are (a)–(d) 22 and (e), (h) 14. The dashed black and gray lines correspond to simulated spectra forced with S_{in}^S and S_{in}^Y , respectively. The black and gray arrows show the wind direction from the measurements and the objective analysis, respectively.

where $\theta = 0^\circ$ corresponds to the dominant wave direction and $\theta_1(k)$ and $\theta_2(k)$ are the azimuthal locations of the maxima on each side of the spectrum. The terms θ_{lobe} and r_{lobe} are shown in Figs. 11a–f and Figs. 11g–l, corresponding to RFs 05 and 10, respectively. Figs. 11a,d,g,j correspond to the ATM observations and Figs. 11b,e,h,k and 11c,f,i,l correspond to the computed spectra using S_{in}^S and S_{in}^Y , respectively. The computed bimodal separations and amplitudes near full development are in good agreement with the computations by AB03 under idealized conditions using S_{in}^S . For both research flights,

the separation and relative amplitude of the lobes for wavenumbers larger than the spectral peak are both larger in the observed spectra than the simulations. However, both simulated and measured spectra show a consistent trend where θ_{lobe} and r_{lobe} decrease with increasing wave age. RM10 showed a collapse of the trend in θ_{lobe} and r_{lobe} for the GOTEX measurements by scaling both parameters with $(c_p/u_*)^{1/2}$. Figure 12 shows the scaled bimodal separation $\theta'_{lobe} = 0.2(c_p/u_*)^{1/2}\theta_{lobe}$; θ'_{lobe} collapses for both sets of computed spectra but is consistently lower than the binned averages of the ATM

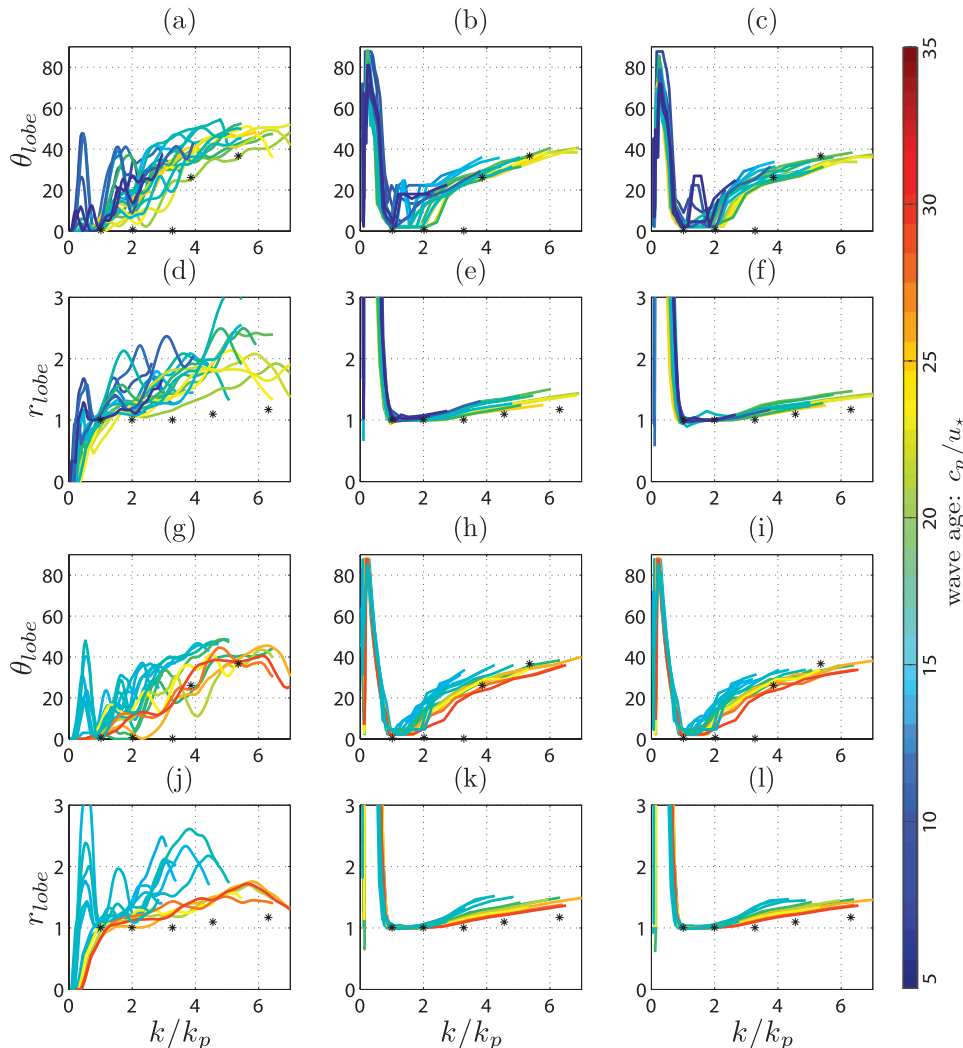


FIG. 11. Bimodal separation θ_{lobe} and relative amplitude r_{lobe} for RFs (a)–(f) 05 and (g)–(l) 10. (a),(d),(g),(j) correspond to the ATM observations; (b),(e),(h),(k) correspond to the computed spectra using S_{in}^S ; and (c),(f),(i),(l) correspond to the computed spectra using S_{in}^Y . The black asterisks show to the computations by AB03 using the wind input function S_{in}^S near full development. See color bar in Fig. 6.

observations reported by RM10, which are shown with solid black lines.

g. Transition between equilibrium and saturation range

As shown in appendix A, the function used to enable the dissipation function at high wavenumbers was designed to approach unity at $k_{oz} = 2k_{zu}$, where k_{zu} corresponds to the zero-up crossing of $S_{nl}(k)$. Figure 13 shows k_{oz}/k_p plotted against the wave age and is compared to the empirically determined transitional wavenumber component (k_o/k_p), between the equilibrium and the saturation ranges of the spectrum (RM10). The simulations show an increase of k_{oz}/k_p with increasing wave age. The computations using S_{in}^S give larger values

of k_{oz}/k_p than those from the simulations with S_{in}^Y and show good agreement with the best-fit estimates of k_o/k_p from RM10 (see also Fig. 6).

5. Discussion and conclusions

This study is concerned with the performance of a modified AB03 dissipation function with a two-regime behavior. At low to intermediate wavenumbers the dissipation corresponds to the model of AB03, at high wavenumbers the dissipation is designed to force the solution to match the observations with an explicit source term balance. The model is compared to field observations of fetch-limited waves under strong wind forcing in the Gulf of Tehuantepec. This study used the wind-wave

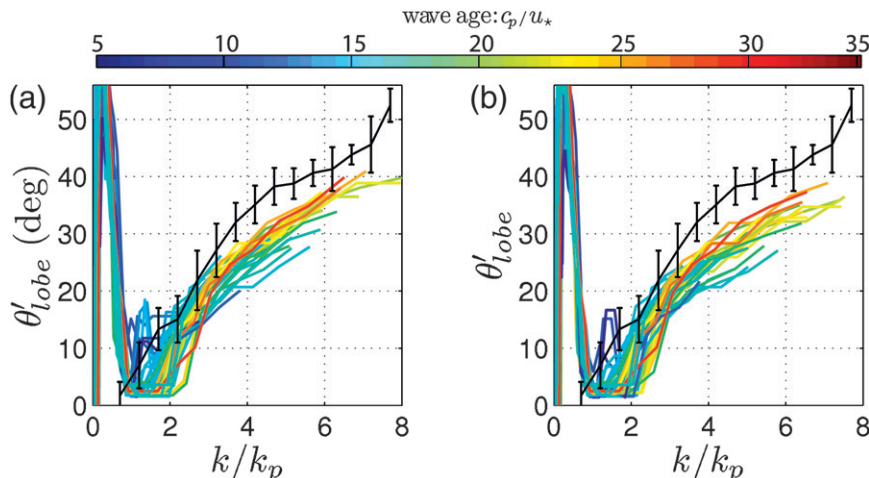


FIG. 12. Scaled bimodal separation [$\theta'_{lobe} = 0.2 \theta_{lobe} (c_p/u_{*2})^{1/2}$] for combined RFs 05 and 10 data for the simulations using the wind input function by (a) Snyder et al. (1981) and (b) Yan (1987). The black lines correspond to the bin-averaged data from measured ATM spectra for RF 05 and 10, with error bars corresponding to one standard deviation.

model WaveWatch III as the numerical framework for the simulations. All model runs were carried out with exact computations of the nonlinear energy transfer resulting from wave–wave interactions, as described by Tracy and Resio (1982) and van Vledder (2006). The wind input functions considered are Snyder et al. (1981) or Yan (1987). The model was tuned and tested in one-dimensional runs against the empirical fetch relationships for stable atmospheric stratification (Kahma and Calcoen 1992). Finally, the model was used for two-dimensional simulations over the Gulf of Tehuantepec. The friction velocities used as input for the model were calculated from measurements at low altitudes (30–50 m above mean sea level) and QuikSCAT winds or NCEP/NARR model winds. The resulting two-dimensional average friction velocity maps show a two-dimensional wind-jet pattern, which was assumed to be in steady state throughout the model computations.

The simulated wave height and dominant wave period are in good agreement with the ATM observations, with rms errors ranging between 5% and 12%. In contrast, the comparison between the observations and the simulations for higher moments of the spectrum is encouraging but not completely satisfactory. The numerical simulations maintain power-law behaviors within the tail of the omnidirectional and k_1 spectra, which are consistent with the observations. The computed omnidirectional spectra exhibits two power laws, an equilibrium range, with $\phi \propto k^{-5/2}$, and a saturation range, with $\phi \propto k^{-3}$. As shown in appendix B, the magnitude of nonlinear energy fluxes is significantly reduced between the equilibrium and saturation ranges when compared to the wind input. The dominant balance within the

saturation range is between S_{in} and S_{ds} , which is consistent with the common assumption used in several investigations (Kudryavtsev et al. 1999; Donelan 1987; Phillips 1984). It is also found that the transition to saturation of the simulated spectra forced with S_{in}^S is in very good agreement with the empirical estimates from RM10. The model spectra forced with S_{in}^Y transition at much smaller wavenumbers. The energy density within the equilibrium range is overestimated in all simulations; the model runs forced with S_{in}^Y give the best results with rms errors between 20% and 60%. This suggests

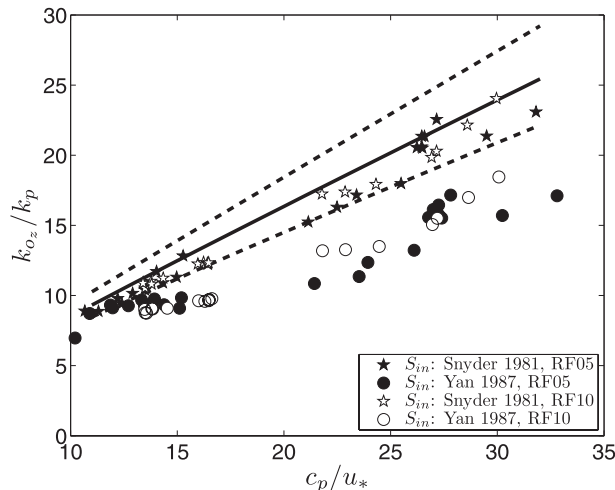


FIG. 13. Wavenumber component k_{oz} corresponding to the beginning of the explicitly balanced dissipation regime, where k_{oz} is normalized by the peak wavenumber k_p and plotted against the wave age. The solid and dashed lines correspond to the best-fit estimate and 95% confidence intervals of k_o/k_p from the field data (RM10).

that at such scales the dissipation must be larger to improve the agreement with the observations.

Another shortcoming of the model is the directional spreading of the simulated spectra being narrower than the observations by about 10° . This is consistent in all simulations, regardless of the parameterization of the wind input used. Similarly, the spectral width in the direction orthogonal to the dominant wave direction (σ_2) from computed spectra is always narrower than the field observations. The wind input parameterization by Janssen (1991), which gives similar growth rates to S_{in}^Y for strongly forced waves, was not used in this study. However, as shown by AB03, the wind input function by Janssen (1991), which has a $\cos^2\theta$ dependence relative to the wind, would produce even narrower directional distributions when compared to computed spectra using S_{in}^Y and S_{in}^S that have a $\cos\theta$ dependence. This suggests that the model dissipation would need to have a narrower azimuthal spreading, as opposed to isotropic, for the model to simulate broader spectra similar to the observations.

An interesting result is the characterization of the bimodal distribution with increasing wave age. Although the measurements show wider lobe separations and larger lobe amplitudes when compared to the simulations, the empirical scaling found in the measurements (RM10), where θ_{lobe} collapses when scaled with $(c_p/u_*)^{1/2}$, was also found to apply for the computed spectra, regardless of the wind input parameterization used.

Some of the problems associated with the AB03 dissipation function have been associated with missing physics, as described by van der Westhuysen et al. (2007). It is argued that the formulation does not account for the breaking probability threshold reported by Banner et al. (2002) nor the cumulative effect of the dissipation at high frequencies resulting from modulations induced by the straining by the longer dominant waves (Donelan 2001; Young and Babanin 2006). Other possible reasons for the discrepancies between the observations and the numerical simulations are the effects of currents, the uncertainties in the wind input and the stationarity of the winds, including wind gustiness. However, as pointed out by an anonymous reviewer, the only available model for gustiness (Abdalla and Cavaleri 2002) gives negligible effects for developing waves. Additionally, as shown in appendix C, the wind input functions considered would not satisfy the momentum budget suggested by the laboratory measurements by Banner and Pierson (1998).

Acknowledgments. We thank Bruce Couruelle and Caroline Papadopoulos for allowing us to carry out the simulations on the computer cluster at Scripps Institution of Oceanography. LR is thankful to Jose Henrique Alves for useful suggestions on the choice of numerical frame-

work for the simulations. LR is thankful to Jessica M. Kleiss for her comments on this manuscript. We thank the anonymous reviewers whose comments and questions have led to significant improvements in this paper. This work was supported by grants to WKM from the National Science Foundation, the Office of Naval Research, and BP.

APPENDIX A

Implementation of Dissipation Function

a. Dissipation regimes

The dissipation function for the two regimes in Eq. (7) was implemented with the following functions:

$$Y_l(k, k_{zu}) = 1 - \tanh\left(\frac{2k}{k_{zu}}\right)^8 \quad \text{and} \quad (\text{A1})$$

$$Y_h(k, k_{zu}) = 1 - Y_l(k, k_{zu}), \quad (\text{A2})$$

where k_{zu} corresponds to the zero-up crossing of the azimuth-integrated nonlinear energy fluxes $S_{\text{nl}}(k) = \int_{-\pi}^{\pi} S_{\text{nl}}(k, \theta)k d\theta$. As shown in Fig. A1, Eqs. (A1) and (A2) provide a sharp transition between the two dissipation regimes. Here, Y_h approximately reaches unity at $k/k_{zu} = 2$, thus the beginning of the saturation range k_{oz} can be defined as $k_{\text{oz}} = 2k_{zu}$.

b. Stability of the saturation range with explicit source term balance

The amplification function H in Eq. (15) was implemented according to

$$H(B) = \left(\frac{B}{\bar{B}}\right)^j, \quad (\text{A3})$$

where B is the azimuth-integrated saturation $\phi(k)k^3$, \bar{B} is the empirical degree of saturation (RM10), and j is a small positive factor. It was found empirically that $j = 0.01$ gives a good convergence rate. Here, it is shown that a small perturbation in the spectrum away from the empirical saturation will generally decay exponentially with time.

We begin by integrating the radiative transport Eq. (1) in azimuth, and rewriting it in terms of the wavenumber saturation (B) gives

$$\frac{dB}{dt} = [S_{\text{in}}(B) + S_{\text{nl}}(B)][1 - H(B, \bar{B})] \quad (\text{A4})$$

$$= S^+(B)[1 - H(B, \bar{B})], \quad (\text{A5})$$

where S^+ is defined as the sum of the azimuth-integrated wind input and the nonlinear energy fluxes. If B is perturbed away from the empirical value \bar{B} by an amount B' ,

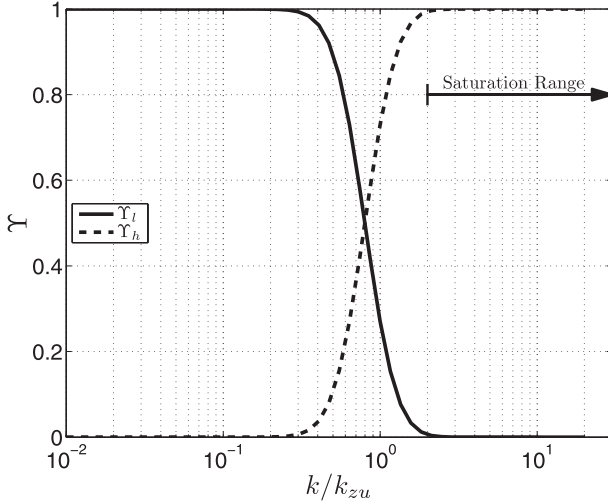


FIG. A1. Functions Υ_l and Υ_h used to enable or disable the dissipation functions S_{ds}^l and S_{ds}^h , respectively, in Eq. (7); k_{zu} is the zero-up crossing of the azimuth-integrated nonlinear transfers $S_{nl}(k)$.

such that $B = \bar{B} + B'$, the expansion of Eq. (A5) about \bar{B} yields

$$\frac{dB'}{dt} = \left[S^+(\bar{B}) + \left(\frac{\partial S^+}{\partial B} \Big|_{B=\bar{B}} \right) B' \right] \left(-\frac{\partial H}{\partial B} B' \right), \quad (A6)$$

which is stable provided that $\partial H/\partial B$ and $S^+(\bar{B})$ are both positive, and $(\partial S^+/\partial B|_{B=\bar{B}}) B' < -S^+(\bar{B})$. Because S^+ is positive within the saturation range, according to Eqs. (A3) and (A6), any small perturbation B' away from the empirical saturation \bar{B} will decay approximately according to

$$\frac{dB'}{dt} \approx -jS^+(\bar{B})B'. \quad (A7)$$

APPENDIX B

Source Term Balance in Equilibrium and Saturation Ranges

Figure A2 shows an example of the azimuth-integrated source term functions S_{in} , S_{ds} , S_{nl} , and S_{tot} , where $S_{tot} = S_{in} + S_{ds} + S_{nl}$. Near the spectral peak, all three terms are comparable in magnitude, but at higher wavenumbers the overall magnitude of S_{nl} and S_{tot} become much smaller than that of S_{in} and S_{ds} . To analyze the source term balance with different parts of the spectrum, we define the beginning of the equilibrium range at $2.25 k_p$ or $1.5 f_p$ (cf. Donelan et al. 1985) and the upper limit at the zero-up crossing of the nonlinear energy fluxes k_{zu} , which is also the lower limit of the saturation range (see discussion in section 3). The energy transport equation integrated in the azimuth is given by

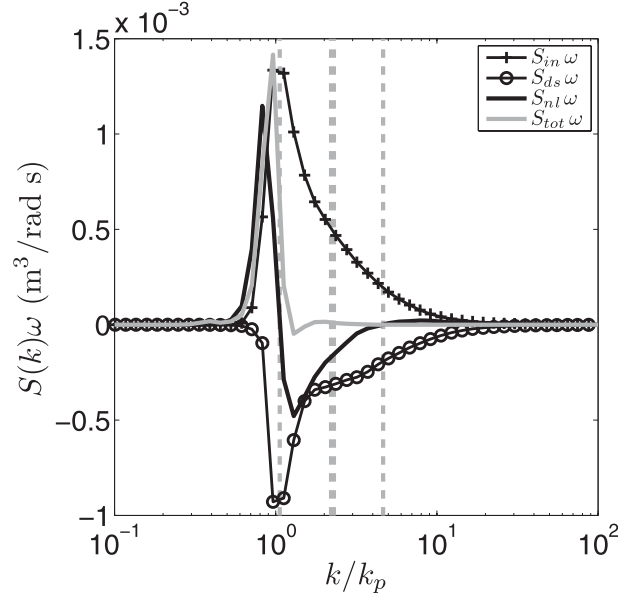


FIG. A2. Sample omnidirectional source terms from the two-dimensional simulations for RF 05 using the wind input by Yan (1987). Here, $S(k) = \int_{-\pi}^{\pi} S(k, \theta) k d\theta$; the thin dashed lines show the zero-down and zero-up crossing of the nonlinear energy fluxes; and the thick dashed line shows $k/k_p = 2.25$, which is often assumed to correspond to the beginning of the equilibrium range in empirical investigations (Donelan et al. 1985; Resio et al. 2004; RM10). The local wave age is $c_p/u_* = 15$.

$$\frac{DN(k)}{Dt} \omega = [S_{in}(k) + S_{nl}(k) + S_{ds}(k)] \omega, \quad (B1)$$

where the term of the left-hand side is the total derivative, defined as the wave production.

Figures A3a–c show the maximum value of each term in Eq. (B1) within the equilibrium range relative to the maximum of the wind input. The terms \mathcal{I}_{me} , \mathcal{N}_{me} , \mathcal{D}_{me} , and \mathcal{P}_{me} correspond to the maximum of the wind input, nonlinear resonant interactions, dissipation, and wave production, respectively, within the equilibrium range. In this range, the dissipation, nonlinear energy fluxes, and production have a magnitude of approximately 70%, 30%, and 5%, respectively, relative to the wind forcing, roughly satisfying the criteria assumed by Phillips (1985). Similarly, within the saturation range, the maximum values of the azimuth-integrated energy source terms are defined as \mathcal{I}_{ms} , \mathcal{N}_{ms} , \mathcal{D}_{ms} , and \mathcal{P}_{ms} , corresponding to the wind input, nonlinear energy flux, dissipation, and wave production, respectively. According to Fig. A3d, the dominant forcing within the saturation range is between the wind input and the dissipation (Kudryavtsev et al. 1999; Donelan 1987; Phillips 1984), because the production (not shown) and the nonlinear energy fluxes are small compared to the wind forcing and dissipation.

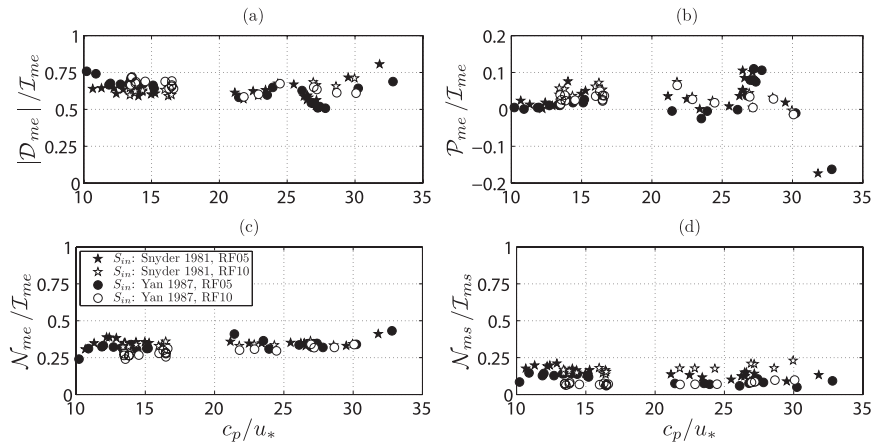


FIG. A3. Source term balance within the (a)–(c) equilibrium and (d) saturation ranges of the spectrum. The maximum forcings within the equilibrium range for $2.25k_p > k > k_{zu}$ are shown, which are the (a) wave dissipation D_{me} , (b) wave production P_{me} , and (c) nonlinear energy flux N_{me} , maximum nonlinear energy transfer flux N_{ms} , all normalized by the maximum of the wind input I_{ms} and plotted against the wave age. (d) The maximum nonlinear energy transfer flux N_{ms} normalized by maximum of the wind input I_{ms} within the saturation range of the spectrum for $k > 2k_{zu}$, where k_{zu} corresponds to the zero-up crossing of the nonlinear energy fluxes.

APPENDIX C

Momentum Balance

a. Energy partition

Based on field observations of the evolution of wind waves (Donelan et al. 1992), as well as field and laboratory measurements of the wind input (Donelan 1987), Donelan (1998) suggests that the energy retained by the

wave field is largest for young waves, reaching up to 4% of the total energy supplied by the wind, and decreasing to zero for fully developed seas. Figure A4 shows the energy retained by the wave field P normalized by the net wind input I , calculated according to Eqs. (C1) and (C2), and plotted versus the local wave age:

$$P = \int_0^{2\pi} \int_{k_o}^{k_f} \frac{DF(k, \theta)}{Dt} k dk d\theta \quad \text{and} \quad (C1)$$

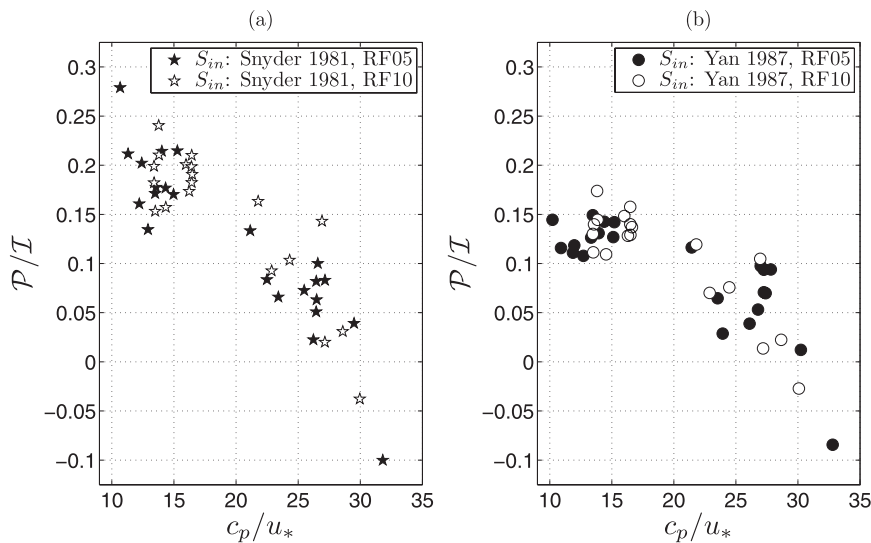


FIG. A4. Energy retained by the wave field P relative to the net wind forcing I vs the wave age for simulations using the wind input by (a) Snyder et al. (1981) and (b) Yan (1987).

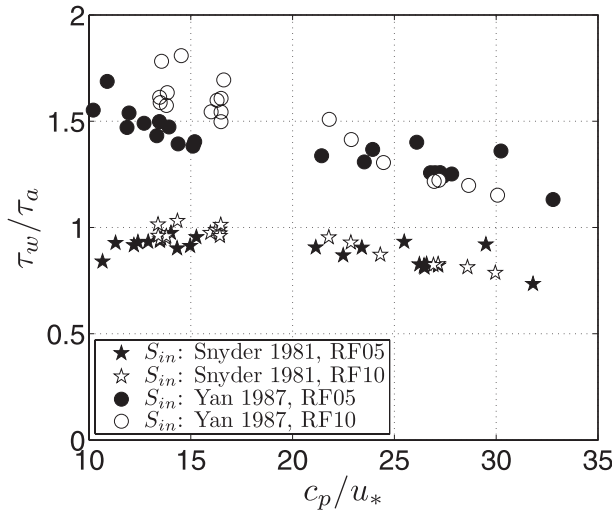


FIG. A5. Ratio of the wave-induced stress τ_w to the total wind stress τ_a as a function of the local wave age.

$$\mathcal{I} = \int_0^{2\pi} \int_{k_o}^{k_f} S_{in}(k, \theta) k dk d\theta. \quad (C2)$$

All of the simulations show that the relative wave production (P/I) decreases with increasing fetch and is greatest using the wind input by Snyder et al. (1981). This is expected, because the wind input by Yan (1987) gives larger net wind inputs. For very old waves ($c_p/u_* > 30$), the production becomes very small, even negative. This is due to the reduction of friction velocity with increasing fetch.

b. Momentum balance

According to the conservation of momentum,

$$\tau_a = \tau_w + \tau_t, \quad (C3)$$

where τ_a , τ_w , and τ_t are the wind, wave-induced, and tangential stress. Figure A5 shows the ratio of the wave-induced stress τ_w to the total wind stress $\tau_a = \rho_a u_*^2$ as a function of the local wave age:

$$\tau_w = \rho_w g \int_{-\pi}^{\pi} \int_{k_o}^{k_f} \frac{S_{in} \cos \theta_w}{c} k dk d\theta, \quad (C4)$$

where $k_o = 0.007$ and $k_f = 20 \text{ rad m}^{-1}$, before the gravity-capillary range, and θ_w is the wind direction. Although the simulations using the wind input by Yan (1987) clearly violate the conservation of momentum, the simulations with the forcing by Snyder et al. (1981) approximately conserve momentum, with τ_w/τ_a mostly less than unity. However, laboratory experiments by Banner and Pierson (1998) suggest that the net tangential stress

should be around 30% of the net momentum flux. This condition is clearly violated by both models, but the direct applicability of laboratory measurements of the partitioning of fluxes to the field has never been demonstrated.

REFERENCES

- Abdalla, S., and L. Cavaleri, 2002: Effect of wind variability and variable air density on wave modeling. *J. Geophys. Res.*, **107**, 3080, doi:10.1029/2000JC000639.
- Alves, J. H. G. M., and M. L. Banner, 2003: Performance of a saturation-based dissipation-rate source term in modeling the fetch-limited evolution of wind waves. *J. Phys. Oceanogr.*, **33**, 1274–1298.
- , D. Greenslade, and M. L. Banner, 2002: Impact of a saturation-dependent dissipation source function on operational hindcasts of wind waves in the Australian region. *Global Atmos. Ocean Syst.*, **8**, 239–267.
- , M. L. Banner, and I. R. Young, 2003: Revisiting the Pierson–Moskowitz asymptotic limits for fully developed wind waves. *J. Phys. Oceanogr.*, **33**, 1301–1323.
- Ardhuin, F., T. H. C. Herbers, K. P. Watts, G. P. V. Vledder, R. Jensen, and H. Graber, 2007: Swell and slanting fetch effects on wind wave growth. *J. Phys. Oceanogr.*, **37**, 908–931.
- , F. Collard, B. Chapron, P. Queffeulou, J.-F. Filipot, and M. Hamon, 2008: Spectral wave dissipation based on observations: A global validation. *Proc. Chinese-German Joint Symp. on Hydraulic and Ocean Engineering*, Darmstadt, Germany, 393–402.
- Babanin, A. V., and A. J. van der Westhuysen, 2008: Physics of saturation-based dissipation functions proposed for wave forecast models. *J. Phys. Oceanogr.*, **38**, 1831–1841.
- Badulin, S. I., A. N. Pushkarev, D. Resio, and V. E. Zakharov, 2005: Self-similarity of wind-driven seas. *Nonlinear Processes Geophys.*, **12**, 891–945.
- Banner, M. L., 1990: Equilibrium spectra of wind waves. *J. Phys. Oceanogr.*, **20**, 966–984.
- , and I. R. Young, 1994: Modeling spectral dissipation in the evolution of wind waves. Part I: Assessment of existing model performance. *J. Phys. Oceanogr.*, **24**, 1550–1570.
- , and W. L. Pierson, 1998: Tangential stress beneath wind-driven air-water interfaces. *J. Fluid Mech.*, **364**, 115–145.
- , and R. Morrison, 2006: On modeling spectral dissipation due to wave breaking for ocean wind waves. *Proc. Ninth Int. Workshop on Wave Hindcasting and Forecasting*, Victoria, BC, Canada, Environment Canada, 1–12.
- , J. Gemmrich, and D. Farmer, 2002: Multiscale measurements of ocean wave breaking probability. *J. Phys. Oceanogr.*, **32**, 3364–3375.
- Bretherton, F. P., R. E. Davis, and C. B. Fandry, 1976: A technique for the objective analysis and design of oceanographic experiments applied to mode-73*. *Deep-Sea Res.*, **23**, 559–582.
- Burgers, G., and V. K. Makin, 1993: Boundary-layer model results for wind-sea growth. *J. Phys. Oceanogr.*, **23**, 372–385.
- Chalikov, D. V., 1986: Numerical simulation of the boundary layer above waves. *J. Fluid Mech.*, **34**, 63–98.
- , and M. Y. Belevich, 1993: One-dimensional theory of the wave boundary layer. *Bound.-Layer Meteor.*, **63**, 65–96.
- Donelan, M. A., 1982: The dependence of aerodynamic drag coefficient on wave parameters. *Proc. First Int. Conf on Meteorology and Air/Sea Interactions of the Coastal Zone*, The Hague, Netherlands, Amer. Meteor. Soc., 2.6.

- , 1987: The effect of swell on the growth of wind waves. *Johns Hopkins APL Tech. Dig.*, **8**, 18–23.
- , 1998: Air-water exchange processes. *Physical Processes in Lakes and Oceans: Lake Biwa, Japan*, J. Imberger, Ed., Coastal Estuarine Series, Vol. 48, Amer. Geophys. Union, 18–36.
- , 2001: A nonlinear dissipation function due to wave breaking. *Proc. Workshop on Ocean Wave Forecasting*, Reading, United Kingdom, ECMWF, 87–94.
- , J. Hamilton, and W. H. Hui, 1985: Directional spectra of wind-generated waves. *Philos. Trans. Roy. Soc. London*, **315A**, 509–562.
- , M. Skafel, H. Graber, P. Liu, D. Schwab, and S. Venkatesh, 1992: On the growth rate of wind-generated waves. *Atmos. Ocean*, **30**, 457–478.
- Evans, K. C., 1998: Observations of the directional spectrum of fetch-limited waves. *J. Phys. Oceanogr.*, **28**, 495–512.
- Friehe, C. A., D. Khelif, and W. K. Melville, 2006: Aircraft air-sea flux measurements in the Gulf of Tehuantepec. Preprints, *14th Conf. on Interaction of the Sea and Atmosphere*, Atlanta, GA, Amer. Meteor. Soc., 7.2.
- Hasselmann, K., 1962: On the non-linear energy transfer in a gravity-wave spectrum. Part 1: General theory. *J. Fluid Mech.*, **12**, 481–500.
- , 1963: On the non-linear energy transfer in a gravity wave spectrum. Part 2: Conservation theorems; wave-particle analogy; irreversibility. *J. Fluid Mech.*, **15**, 273–282.
- , 1974: On the spectral dissipation of ocean waves due to white capping. *Bound.-Layer Meteor.*, **6**, 107–127.
- , and Coauthors, 1973: Measurements of wind-wave growth and swell decay during the Joint North Sea Wave Project (JONSWAP). *Dtsch. Hydrogr. Z.*, **8**, 1–95.
- Hasselmann, S., and K. Hasselmann, 1985: Computation and parameterizations of the nonlinear energy transfer in a gravity-wave spectrum. Part II: Parameterizations of the nonlinear energy transfer for application in wave models. *J. Phys. Oceanogr.*, **15**, 1378–1391.
- Hwang, P., D. Wang, E. Walsh, W. Krabill, and R. Swift, 2000: Airborne measurements of the wavenumber spectra of ocean surface waves. Part II: Directional distribution. *J. Phys. Oceanogr.*, **30**, 2768–2787.
- Janssen, P. A. E. M., 1989: Wave-induced stress and the drag of air flow over sea waves. *J. Phys. Oceanogr.*, **19**, 745–754.
- , 1991: Quasi-linear theory of wind wave generation applied to wave forecasting. *J. Phys. Oceanogr.*, **21**, 1631–1642.
- , 2003: Nonlinear four-wave interactions and freak waves. *J. Phys. Oceanogr.*, **33**, 863–884.
- Kahma, K. K., and C. J. Calkoen, 1992: Reconciling discrepancies in the observed growth of wind-generated waves. *J. Phys. Oceanogr.*, **22**, 1389–1405.
- Komen, G. J., S. Hasselmann, and K. Hasselmann, 1984: On the existence of a fully developed wind-sea spectrum. *J. Phys. Oceanogr.*, **14**, 1271–1285.
- Krasitskii, V. P., 1994: On reduced equations in the Hamiltonian theory of weakly nonlinear surface waves. *J. Fluid Mech.*, **272**, 1–20.
- Kudryavtsev, V., V. Makin, and B. Chapron, 1999: Coupled sea surface-atmosphere model. 2. Spectrum of short wind waves. *J. Geophys. Res.*, **104**, 7625–7639.
- Large, W. G., and S. Pond, 1982: Sensible and latent heat flux measurements over the ocean. *J. Phys. Oceanogr.*, **12**, 464–482.
- Lavrenov, I. V., 2001: Effect of wind wave parameter fluctuation on the nonlinear spectrum evolution. *J. Phys. Oceanogr.*, **31**, 861–873.
- Lewis, A., and R. Allos, 1990: JONSWAP's parameters: Sorting out inconsistencies. *Ocean Eng.*, **17**, 409–415.
- Miles, J. W., 1957: On the generation of surface waves by shear flow. *J. Fluid Mech.*, **3**, 185–204.
- Perlin, N., R. M. Samelson, and D. B. Chelton, 2004: Scatterometer and model wind and wind stress in the Oregon–northern California coastal zone. *Mon. Wea. Rev.*, **132**, 2110–2129.
- Phillips, O. M., 1984: On the response of short ocean wave components at a fixed wavenumber to ocean current variations. *J. Phys. Oceanogr.*, **14**, 1425–1433.
- , 1985: Spectral and statistical properties of the equilibrium range in wind-generated gravity waves. *J. Fluid Mech.*, **156**, 505–531.
- Pierson, W., Jr., and L. Moskowitz, 1964: A proposed spectral form for fully-developed wind seas based on the similarity theory of S. A. Kitaigorodskii. *J. Geophys. Res.*, **69**, 5181–5190.
- Plant, W. J., 1982: A relationship between wind stress and wave slope. *J. Geophys. Res.*, **87**, 1961–1967.
- Pushkarev, A., D. Resio, and V. Zakharov, 2003: Weak turbulent approach to the wind-generated gravity sea waves. *Physica D*, **184**, 29–63.
- Resio, D. T., and W. Perrie, 1991: A numerical study of nonlinear energy fluxes due to wave-wave interactions. Part 1: Methodology and basic results. *J. Fluid Mech.*, **223**, 609–629.
- , C. E. Long, and C. L. Vincent, 2004: The equilibrium-range constant in wind-generated wave spectra. *J. Geophys. Res.*, **109**, CO1018, doi:10.1029/2003JC001788.
- Romero, L., 2008: Airborne observations and numerical modeling of fetch-limited waves in the Gulf of Tehuantepec. Ph.D. thesis, University of California, San Diego, 111 pp.
- , and W. K. Melville, 2010: Airborne observations of fetch-limited waves in the Gulf of Tehuantepec. *J. Phys. Oceanogr.*, **40**, 441–465.
- Snyder, R. L., F. Dobson, J. Elliott, and R. B. Long, 1981: Array measurements of atmospheric pressure fluctuations above surface gravity waves. *J. Fluid Mech.*, **102**, 1–59.
- Tolman, H. L., 2002: User manual and system documentation of Wavewatch-III, version 2.22. NOAA/NWS/NCEP/MMAB Tech. Note 222, 133 pp.
- , and D. Chalikov, 1996: Source terms in a third-generation wind wave model. *J. Phys. Oceanogr.*, **26**, 2497–2518.
- Tracy, B. A., and D. T. Resio, 1982: Theory and calculation of the nonlinear energy transfer between sea waves in deep water. U.S. Army Engineer Waterways Experiment Station Tech. Rep. 11, 47 pp.
- van der Westhuysen, A. J., M. Zijlema, and J. A. Battjes, 2007: Saturation-based whitecapping dissipation in SWAN for deep and shallow water. *Coastal Eng.*, **54**, 151–170.
- van Vledder, G. P., 2006: The WRT method for the computation of non-linear four-wave interactions in discrete spectral wave models. *Coastal Eng.*, **53**, 223–242.
- Webb, D., 1978: Non-linear transfers between sea waves. *Deep-Sea Res.*, **25**, 279–298.
- Yan, L., 1987: An improved wind input source term for third generation ocean wave modelling. Royal Netherlands Meteorological Institute Scientific Rep. WR-87-9, 10 pp.
- Young, I. R., and G. P. V. Vledder, 1993: A review of the central role of nonlinear interactions in wind-wave evolution. *Philos. Trans. Roy. Soc. London*, **342A**, 505–524.
- , and A. V. Babanin, 2006: Spectral distribution of energy dissipation of wind-generated waves due to dominant wave breaking. *J. Phys. Oceanogr.*, **36**, 376–394.